Journal of The Electrochemical Society, **165** (14) D774-D782 (2018)
0013-4651/2018/165(14)/D774/9/$37.00 © The Electrochemical Society

The Effect of SiC Nanoparticle Size on the Electrodeposition of Zn–SiC Nanocomposite Coatings from Citrate Bath

Honorata Kazimierczak,[1,2,*,z] Krzysztof Szymkiewicz,[2] Piotr Bobrowski,[2] Zbigniew Świątek,[2] Łukasz Rogal,[2] Eliezer Gileadi,[3,] and Noam Eliaz[1,*]**

[1] *Biomaterials & Corrosion Laboratory, Department of Materials Science and Engineering, Tel-Aviv University, Ramat Aviv 6997801, Israel*
[2] *Institute of Metallurgy and Material Science, Polish Academy of Sciences, 30-059 Krakow, Poland*
[3] *School of Chemistry, Faculty of Exact Sciences, Tel-Aviv University, Ramat Aviv 6997801, Israel*

A comparison is made between the codeposition behavior of Zn with SiC nanoparticles (NPs) of two average sizes: 56 nm and 90 nm. The SiC NPs are first characterized using transmission electron microscopy (TEM) and X-ray diffraction (XRD). Dynamic light scattering (DLS) is used to compare the surface charge of both kinds of SiC NPs suspended in aqueous citrate electrolytes. The effect of applied current density, hydrodynamic conditions, and total charge passed on the SiC content in the coating and electrodeposition rate is studied. The electrodeposited Zn-SiC coatings are characterized by wavelength dispersive X-ray fluorescence (WDXRF), scanning electron microscopy (SEM), and XRD. The results obtained confirm that Cit-Zn complexes are adsorbed on the surface of the SiC NPs, which are transported to the cathode and are codeposited with Zn during reduction. Zn-SiC incorporation may proceed also by mechanical entrapment of SiC agglomerates in the cavities and pores that are formed in the deposit under condition of relatively fast Zn deposition, which is accompanied by fast hydrogen evolution.
 [DOI: 10.1149/2.1271814jes]

Manuscript submitted August 13, 2018; revised manuscript received November 5, 2018. Published November 15, 2018.

Zinc-based coatings are widely used for cathodic protection of steels from corrosion, due to their low cost and environment compatibility. Research on zinc-based layers with enhanced properties in comparison to pure zinc, such as higher wear resistance, hardness, and corrosion resistance, has been ongoing for several years. The incorporation of a second phase in the form of micro- or nanoparticles (NPs) into a metal matrix may result in a substantial improvement of a variety of properties of the composite material in comparison with a pure metal or alloy.[1,2] Silicon carbide (SiC) micro- and nanosized particles are of considerable interest as a potential reinforcing agent in metal matrix composites (MMCs) due to the advantageous combination of properties, such as high wear, temperature and thermal shock resistance, chemical inertness to all alkaline and acid solutions, and superior hardness.[3–7]

The fabrication of MMCs by electrodeposition has advantages such as ambient pressure and temperature, versatility in producing composite coatings with good quality and well dispersed particles, a smooth surface, and good coating-substrate bonding, in a single step, at low cost, and using an easily controllable and reproducible procedure. Moreover, it can ensure continuous processing and the capability to handle complex geometries.[1,8]

Electrodeposition of MMCs with SiC reinforcement has already been widely studied, mainly with Ni matrices.[4,9–18] There are only a few works dealing with SiC co-electrodeposition with Zn.[5,6,19–26] The microstructure and properties of electrodeposited MMCs with ceramic particles reinforcement are affected by the particle chemistry, size, concentration, dispersion quality, and incorporation rate, as well as by the applied current/potential value and profile, pH, the presence of additives, temperature, and bath stirring.[5,19,21,26–35]

Previously,[26] we proposed aqueous citrate solutions as baths for electrodeposition of Zn-SiC composite coatings, because citrates are non-toxic, form strong complexes with Zn(II), and provide pH stabilization of the electrolyte solutions.[36–38] We investigated, for the first time, the galvanostatic electrodeposition of Zn-SiC from an aqueous citrate bath containing SiC NPs with an average size of 56 nm. It was shown that SiC codeposition with Zn proceeds through the entrapment of ceramic NPs during the reduction of citrate-zinc ions that are first adsorbed on the surface of the ceramic NPs. A maximal content of 6.4 wt% SiC incorporated in the Zn matrix was obtained at the lowest applied current density of $j = -0.5$ A dm^{-2}, with a nearly constant faradaic efficiency of 90%.

In the present paper, we extend our previous study in order to further support and better understand the kinetics and mechanism of electrode processes occurring in the Cit-Zn-SiC aqueous system. To this aim, the effects of the average size of the SiC NPs, applied current density, hydrodynamic conditions, and total charge passed on the codeposition processes are further studied. Furthermore, the surface morphology, microstructure, and phase composition of the composite coatings are characterized.

Materials and Methods

The plating baths were prepared by dissolving sodium citrate (0.25 M) and zinc sulfate (0.20 M) in deionized water, followed by the addition of SiC NPs (60–120 g dm^{-3}) together with gelatin (1 g dm^{-3}) as a surfactant. The solution pH was adjusted to 4.5 by the addition of sulfuric acid. All chemicals used were of analytical grade. Two types of spherical SiC NPs were used: (i) with an average size of 56 nm (supplied by Nanostructured & Amorphous Materials, Inc., Houston, TX), referred to hereafter as SiC(A), and (ii) with an average size of 90 nm (Alpha Aesar), referred to hereafter as SiC(B). The solutions were stirred magnetically for 24 h at 200 rpm before electrochemical deposition, in order to disaggregate and disperse the particles well. The magnetic stirring was maintained also during the electrochemical experiments. All experiments were conducted at room temperature (approximately 20°C).

The electrochemical measurements were performed in a 200 cm^3, three-electrode cell with a RDE (the applied rotation rates were in the range from 150 to 550 rpm), to ensure constant and controlled hydrodynamic conditions, by means of a Metrohm Autolab PGSTAT302N potentiostats/galvanostat. The working electrode was a copper disc placed in a sealed Teflon holder (active surface area 2.83 cm^2). A platinum sheet (3.5 cm^2) was used as a counter electrode. All potentials were measured versus a saturated calomel electrode (SCE). The zeta potential, ζ, of SiC NPs suspended in citrate-based electrolytes was measured using a Zetasizer Malvern ZS system. The zeta potential was obtained from the electrophoretic mobility by the Smoluchowski equation.[39]

The composition of deposits was determined by wavelength dispersive X-ray fluorescence (WDXRF). Analysis was carried out using a Rigaku Primini spectrofluorimeter with scintillation counters (LiF crystal). The weight percentage of SiC in the Zn-SiC composite was

*Electrochemical Society Member.
**Electrochemical Society Fellow.
[z]E-mail: honorata.kazimierczak@gmail.com

calculated from the Zn and Si weight percentages, using Eq. 1:[20]

$$\mathrm{SiC(wt\%)} = \frac{\mathrm{Si\,(wt\%)} + \frac{\mathrm{Si(wt\%)}}{M_{\mathrm{Si}}} \times M_{\mathrm{C}}}{\mathrm{Zn(wt\%)} + \mathrm{Si(wt\%)} + \frac{\mathrm{Si(wt\%)}}{M_{\mathrm{Si}}} \times M_{\mathrm{C}}} \times 100 \qquad [1]$$

where M_{Si} and M_{C} are the atomic masses of silicon and carbon, respectively. The current efficiency of the process was calculated according to Eq. 2:[15]

$$\eta\ (\%) = \frac{m_{\mathrm{Zn}(r)}}{m_{\mathrm{Zn}(t)}} = \frac{\Delta m - \mathrm{SiC\,(wt\%)} \times \Delta m}{k_{Zn}\, Q} \times 100 \qquad [2]$$

where $m_{\mathrm{Zn}(r)}$ is the real mass of the deposited zinc matrix, $m_{\mathrm{Zn}(t)}$ is the theoretical mass of deposited zinc calculated from Faraday's law, Δm is the mass of the deposited composite (Zn-SiC) layer, k_{Zn} is the electrochemical equivalent of Zn (3.39×10^{-4} g C^{-1}), and Q is the charge applied during electrodeposition ($= It$). The Zn deposition rate was calculated from the known deposition time and the mass of deposits (subtracting the mass of SiC incorporated into Zn). The samples were weighed before and after the deposition process using Kern ALT analytical scales with readability of 0.01 mg. The reproducibility of the electrodeposition process was verified using three to five replicates; typical results are reported herein.

SiC nanopowders were imaged in their as-received condition in a Tecnai G2 F20 transmission electron microscope (TEM). The powders were first placed on a copper grid supported by a thin carbon layer. Quantitative analysis of the size distribution of SiC NPs was conducted on TEM images using ImageJ open source image processing program (https://imagej.net/Welcome).

The surface morphology and the microstructure of Zn-SiC composite coatings was studied on metallurgical cross-sections by a FEI model Quanta 3D field-emission gun (FEG) scanning electron microscope (SEM), equipped with an energy-dispersive X-ray spectroscopy (EDS) Trident system (Apollo 40 EDS spectrometer).

X-ray diffraction (XRD) measurements were carried out using a Bruker D8 Discover diffractometer with Co anode ($\lambda = 1.790307$ Å). The measurements were performed in reflection mode with the Bragg–Brentano geometry. The scanning voltage of the X-ray tube was 40 kV, the current was 40 mA, and the measured angle, 2θ, was scanned from 30° to 110° at a scanning step of 0.02°. A highly sensitive Lynx Eye 1-D silicon strip detector was used in a continuous scan mode. Structure refinement was performed using the whole-pattern decomposition (Profile Matching) procedure, also known as LeBail fitting,[40] as implemented in the FullProf program.[41] A single-line analysis was used to determine the crystallite size and crystal lattice deformations.[42] The peak profiles were modelled using the pseudo-Voigt function. The average size of crystallites was estimated from the formula:

$$D_{cryst} = \frac{\lambda}{\beta_C\,(f)\cos\theta} \qquad [3]$$

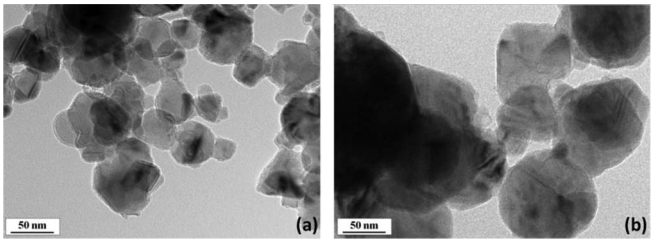

Figure 1. TEM bright-field (BF) images of the spherical β-SiC nanoparticles used in this study. (a) SiC(A), a size range of 7–270 nm, an average of 56 nm. (b) SiC(B), a size range of 11–390 nm, an average of 90 nm.

and the crystal lattice deformation was obtained from the formula:

$$\varepsilon = \frac{\beta_{\mathrm{G}}\,(f)}{4\,\tan(\theta)} \qquad [4]$$

where D_{cryst} is the particle size in nanometers, λ is the wavelength of the $\mathrm{CuK}_{\alpha 1}$ radiation (in nanometers), $\beta_C(f)$ and $\beta_G(f)$ are the Cauchy and Gauss components, respectively, of the actual (physical) broadening of the diffraction line profile, which can be calculated from the formulas:

$$\beta_C\,(f) = \beta_C\,(h) - \beta_C\,(i) \qquad [5]$$

$$\beta_G\,(f) = \sqrt{\beta_G(h)^2 - \beta_G(i)^2} \qquad [6]$$

where $\beta_C(h)$ and $\beta_G(h)$ are the Cauchy and Gaussian components of the broadening of the diffraction line profile designated in the experiment, $\beta_C(i)$ and $\beta_G(i)$ are the Cauchy and Gaussian components of the apparatus broadening of the diffraction line profile, which can be determined from X-ray diffraction measurement of a standard sample (LaB6, NIST Standard Reference Powder 660a).

Results and Discussion

Characterization of the SiC nanoparticles.—Two types of SiC NPs were characterized in their as-received condition before being introduced to the electrolyte solution. These were commercially available β-SiC NPs from two different brands, both with supposedly the same shape and a stated average size of 50 nm. TEM images revealed that in both cases the NPs can be characterized as spheres of a non-uniform size (Fig. 1). However, there is a significant difference in the average particle size of the two nanopowders considered. Analysis of the particle size distribution (Fig. 2) indicates a notable discrepancy in the diameter of the particles in the SiC(B) powder, which contains comparably high amounts of very fine grains with a diameter of about 40 nm and of more coarse grains of about 90 nm. Moreover, the particle size distribution is very broad, ranging from

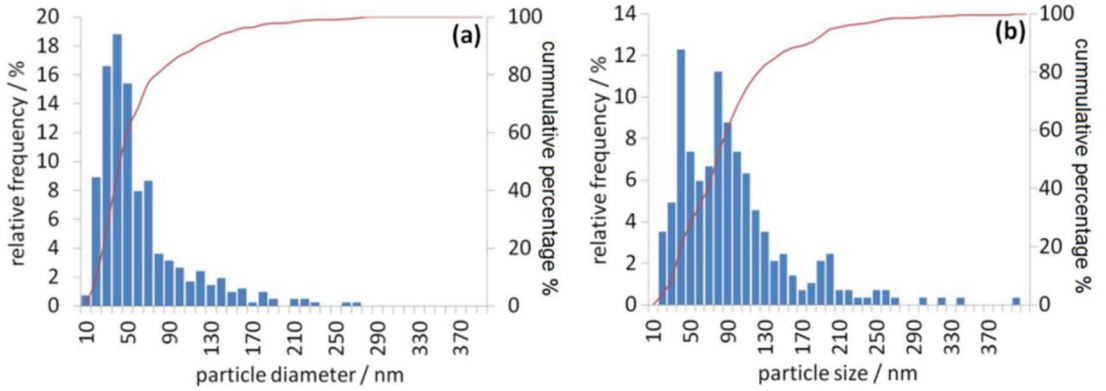

Figure 2. Histograms of the size of the SiC nanoparticles. (a) SiC(A), (b) SiC(B). Corresponding TEM images are shown in Figs. 1a and 1b, respectively.

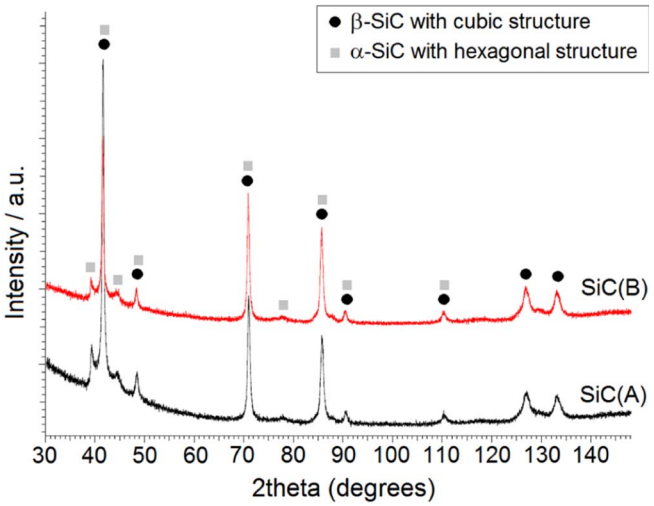

Figure 3. X-ray diffraction patterns of the silicon carbide nanoparticles, SiC(A) and SiC(B), used for electrodeposition of composite coatings. See Figs. 1 and 2 for characterization of their shape and size by TEM.

11 to 390 nm, with an average value of 90 nm (Fig. 2b). On the other hand, the size of SiC(A) is considerably smaller, with diameter values in the range from 7 to 270 nm, and an average value of 56 nm, although the highest relative frequency is noted for particles of about 40 nm (Fig. 2a). XRD measurements (Fig. 3) revealed that the two SiC nanopowders are characterized mainly by the cubic structure of the β-SiC phase, although some peaks corresponding to α-SiC are also visible on the diffractograms, indicating that the NPs used are mixtures of two SiC phases. Hence, the only significant difference is in the particles' average size and distribution, while there are no significant distinctions in the phase composition or shape of the two sets of SiC NPs investigated.

Zeta potential and particle size distribution in suspension.—We previously reported (Fig. 4a in Ref. 26) the dependence of the zeta potential of SiC(A) on the solution chemistry. The zeta potential of SiC NPs suspended in pure deionized water was reported to be around –25 mV. This value was essentially unchanged when gelatin was added, implying that gelatin did not interact with SiC in pure water. The addition of zinc ions in the absence of citrate and gelatin essentially did not affect the measured zeta potential, whereas the addition of citrate ions to the H_2O–SiC system resulted in a slight change of the surface charge to a more negative value (–29 mV). The zeta potential of SiC NPs was most negative (–36 mV) in the Zn–Cit solution.

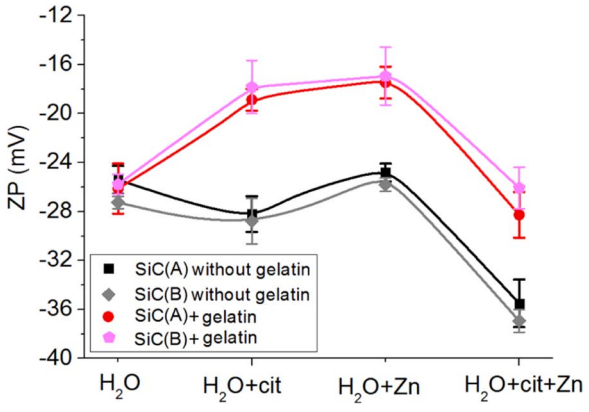

Figure 4. Zeta potential (ZP) of SiC(A) and SiC(B) nanoparticles in a water-based solution containing zinc (0.20 M) and citrate (0.25 M) ions, either separately or together, with and without addition of 1 g dm^{-3} gelatin.

These results clearly indicated the adsorption of negative citrate and zinc-citrate ions onto the surface of the SiC NPs, thus changing their surface charge. Except than in pure water, the addition of gelatin resulted in a shift of the zeta potential to less negative values. This is a proof of the adsorption of gelatin on the surface of the SiC NPs. The zeta potential of SiC increased with the increase of gelatin concentration in the Zn–Cit electrolyte, up to a limiting value of 1.5 g dm^{-3}. In contrast, the increase of the zinc ion and citrate ion concentrations in Zn–Cit electrolytes resulted in a noticeable decrease in the charge of the SiC surface, to more negative values, as long as all zinc and citrate ions were bound to each other in the form of Zn–Cit complex ions. Once there was excess of either free zinc ions or free citrate ions, the zeta potential started to increase (to less negative values). Thus, it was concluded that the negative Cit and Zn–Cit ions as well as positive gelatin fragments were adsorbed on the surface of the SiC NPs in the studied electrolyte solutions.

Here, we can learn from Fig. 4 that the zeta potential of SiC(B) behaves similar to that of SiC(A), both for a given solution or in terms of dependence on the solution chemistry. It can be noticed that the zeta potential registered for SiC(B) NPs is slightly lower in the system without gelatin, and slightly higher in solution with gelatin, both compared to the respective values registered for SiC(A). This implies marginally higher amount of Zn-Cit, Cit and gelatin molecules adsorbing onto the SiC(B) NPs. However, our results indicate that the negatively charged Cit and Zn–Cit ions as well as the positively charged gelatin fragments are adsorbed to the similar extent on the surfaces of SiC(A) and SiC(B) NPs. Hence, it may be argued that the mechanism of adsorption of Cit, Cit–Zn and gelatin molecules is the same on SiC(A) and SiC(B) NPs suspended in water-based citrate solutions.

Electrodeposition of Zn-SiC layers.—The dependence of current density on the composition of the deposited Zn-SiC layers, the current efficiency, and the Zn deposition rate for deposits obtained in the presence of either SiC(A) or SiC(B) nanopowders is shown in Fig. 5. In both cases, the change in the composition of Zn–SiC electrodeposits with applied current density shows the same tendency. When the lowest cathodic current density of j = –0.5 A dm^{-2} is applied, the percentage of SiC incorporated into Zn is the highest, amounting to either 9 or 4.7 wt% for SiC(B) and SiC(A), respectively. This maximum in the incorporation of the ceramic NPs into the metal matrix can be explained by conditions of potential of zero charge, E_{pzc}.[26,43] Further changes in the content of SiC in the deposits with the increase of cathodic current density was previously claimed by us, for SiC(A), to be associated with: activation-controlled reduction of ZnH_2Cit^0 (j from –1.0 to –2.0 A dm^{-2}) and $Zn(HCit)^-$ (j = –3.0 A dm^{-2}), and next with mass transport-limited electrodeposition and intensive hydrogen coevolution (j from –4.0 to –6.0 A dm^{-2}).[26] Herein, it is important to note that the observed dependences are the same for both types of SiC NPs investigated; yet, the content of SiC in the composite coating is noticeably higher when the coarser SiC(B) nanopowder is used. Based on the former comparison, it can be claimed that the mechanism of incorporation of SiC NPs into the Zn matrix is the same for both SiC(A) and SiC(B), namely it proceeds through the entrapment of ceramic NPs during the reduction of Zn–Cit ions that are adsorbed on the surface of the NPs. The observed difference in the concentration (wt%) of SiC in Zn-SiC(A) and Zn-SiC(B) deposits, in the whole range of current densities studied, implies that a comparable number of particles may be incorporated into the zinc matrix in both cases considered. Hence, a possible explanation of the higher total weight percentage of SiC in Zn-SiC(B) deposits may be simply related to the bigger size of the embedded SiC(B) particles, in comparison to a similar number of SiC(A) particles with smaller average size. Furthermore, the smaller the SiC particles, the larger the surface area available for Zn–Cit ion adsorption, when comparing the same concentration of particles suspended in the electrolyte. This explains the difference in the current efficiency values (Fig. 5b) and zinc deposition rates (Fig. 5c), depending on the type of SiC studied, which are observed in

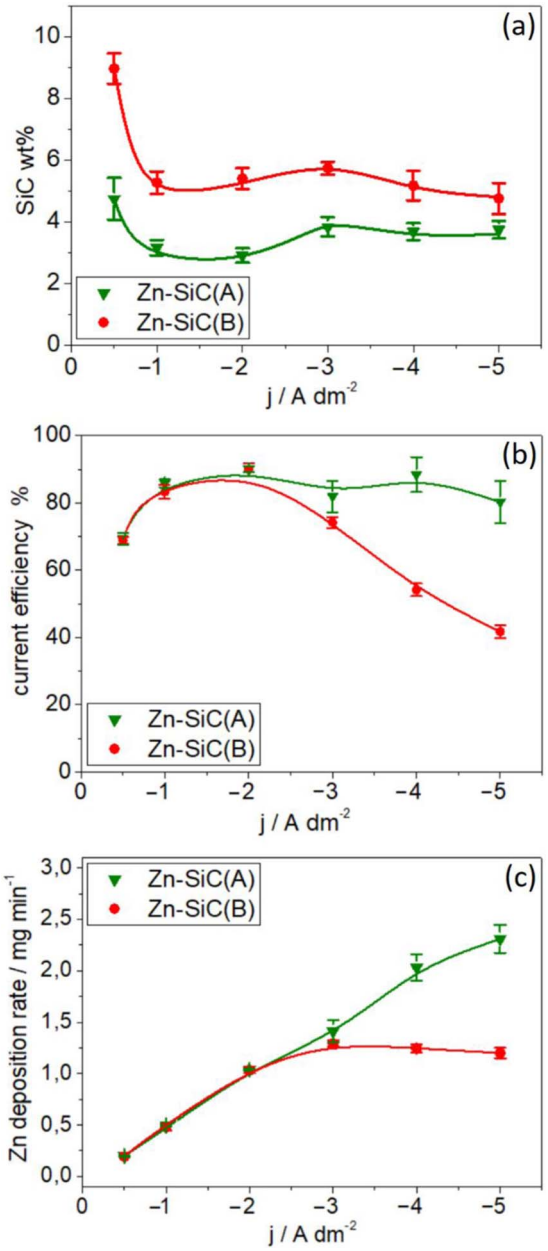

Figure 5. The effect of cathodic current density on: (a) the SiC content in Zn-SiC composite deposits for the two types of SiC nanopowders used, (b) the current efficiency of the electrodeposition process, and (c) the Zn deposition rate. Electrolyte composition: 0.25 M Cit, 0.20 M $ZnSO_4$, 1 g dm^{-3} gelatin, 60 g dm^{-3} SiC. $\omega = 300$ rpm, $Q = 20$ C, $T = 20°C$.

conditions when mass transport begins to be important in the process of zinc electrodeposition. It was claimed previously[44] that at $j = -0.5$ A dm^{-2} the condition of potential of zero charge prevails. Under such condition, the SiC NPs are incorporated into the growing Zn deposit by dispersion forces. Hence, their role as the carrier of electroactive Zn-Cit ions does not affect the kinetics of Zn electrodeposition processes. At cathodic current densities higher than $j = -0.5$ A dm^{-2}, the working electrode becomes polarized negatively, and the electrode processes are activation-controlled under applied current densities of up to –3.0 A dm^{-2}. However, the slight decrease in current efficiency and in deposition rate in the case of the Zn–Cit–SiC(B) system compared to the Zn–Cit–SiC(A) system, at $j = -3.0$ A dm^{-2}, suggests that mass transport influences the control of the electrode processes. It can be speculated that if the larger SiC(B) NPs transport with them less Zn–Cit ions compared to the same concentration of the smaller SiC(A) NPs, then a slight decrease of the Zn deposition rate is expectedly observed in the Zn-SiC(B) system compared to the Zn-SiC(A) system, assuming that mixed activation-diffusion control prevails. Next, under conditions of diffusion-controlled electrodeposition (i.e. when the cathodic current density is increased from –3.0 to –5.0 A dm^{-2}), the SiC(B) NPs surrounded by Zn–Cit ions that reach the cathode's surface do not provide enough electroactive species for the Zn electrodeposition process to occur to the extent observed in the Zn–Cit–SiC(A) system. Moreover, the larger Zn-SiC(B) NPs may block the cathode surface more easily than the smaller SiC(A) NPs, thus hindering more easily the reduction of freely solvated Zn–Cit ions. Consequently, the values of current efficiency and zinc deposition rate are considerably lower in the case of Zn-SiC(B) electrodeposition at high overpotentials. The higher weight percent of SiC NPs in Zn-SiC(B) may also results from this change of the total growth rate of Zn.

In the next step, the effect of RDE speed on the electrodeposition of Zn-SiC(A) and Zn-SiC(B), at three chosen current densities (–0.5, –3.0 and –5.0 A dm^{-2}) is studied (Fig. 6). At –0.5 A dm^{-2}, increase of RDE speed results in the decrease of SiC content in the deposit (Fig. 6a), and in decrease in both the Zn deposition rate and current efficiency (Fig. 6b). This clearly confirms the relation between SiC NPs incorporation and Zn electrodeposition processes under such conditions. When the electrode processes are relatively slow (at $j = -0.5$ A dm^{-2}), the increase of RDE speed may foster the "sweeping" of both ceramic NPs and electroactive Zn–Cit species from the cathode surface so that their residence time becomes too short for the Zn and SiC codeposition processes to proceed fully.

The characteristic difference in the total weight percentage of SiC in the deposits, which as aforementioned is higher for the larger SiC(B) NPs, is maintained at a similar level throughout the whole range of applied RDE speeds (Fig. 6a). However, this difference in the SiC(A) and SiC(B) content incorporated into the Zn matrix is not directly proportional to the difference in average size of these two types of NPs: the SiC(B) wt% is ca. 1.2 times higher than the SiC(A) wt% codeposited with Zn under the same conditions, whereas the SiC(B) NPs average size is ca. 1.6 larger than the average size of SiC(A). Hence, it can be argued that the number of larger SiC(B) NPs codeposited with Zn at $j = -0.5$ A dm^{-2}, from the bath containing 100 g dm^{-3} SiC, is lower than the number of the smaller SiC(A) NPs in Zn-SiC(A) deposits. This suggests that smaller NPs can be more easily buried into the growing Zn matrix as individual particles under such conditions. This indicates that the previous statement arguing that the number of incorporated SiC(A) and SiC(B) NPs is similar does not always apply strictly. Yet, the results presented herein do not contradict the statement that the higher weight percent of SiC in Zn-SiC(B) is due to larger SiC(B) particles, even if the number of SiC(B) particles incorporated into the Zn matrix is slightly lower than in the case of Zn-SiC(A). Moreover, a higher number of the smaller SiC(A) NPs implies that more Zn–Cit ions are transported with them to the cathode surface. Such particles surrounded by Zn–Cit ions then adsorb onto the cathode's surface and may act as nucleation sites for Zn crystallization, which can explain the slightly higher rate of Zn deposition and higher current efficiency in the case of Zn-SiC(A), see Fig. 6b. Such dependency of the Zn deposition rate on the average size of SiC is observed also in the case of electrodeposition at $j = -3.0$ A dm^{-2} at the lowest applied RDE speed (Fig. 6d). However, the Zn deposition rate rises with the increase of RDE speed, and becomes equal for both Zn-SiC(A) and Zn-SiC(B) electrodeposition processes at RDE speeds higher than 150 rpm. The current efficiency of the electrodeposition process also reaches the maximum value of about 90%. On the other hand, the SiC content in Zn-SiC composites decreases with the increase of RDE, after reaching its maximum at 250 rpm. However, the characteristic difference in the content of SiC codeposited with Zn is maintained in the whole range of RDE speeds investigated (Fig. 6c). The Zn deposition rate grows from ca. 0.22 mg min^{-1} at $j = -0.5$ A dm^{-2} (Fig. 6b) to ca. 1.5 mg min^{-1} at $j = -3.0$ A dm^{-2} (Fig. 6d). Under such conditions, when the electrode processes are relatively fast, the rate of mass transport begins to be a

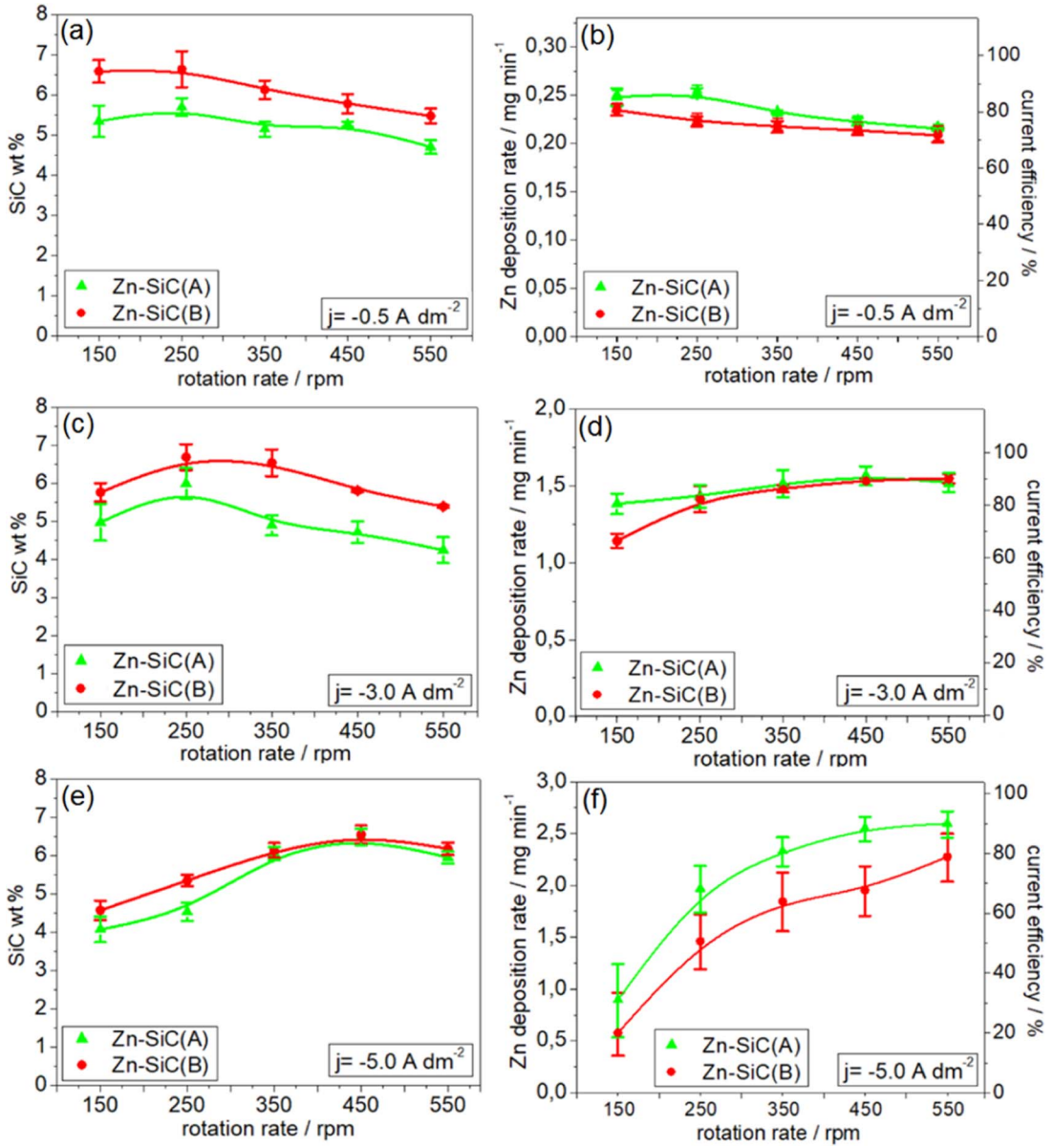

Figure 6. The effect of rotation rate of the rotating disc electrode (RDE) and three current densities on: (a,c,e) the SiC content in Zn-SiC composite deposits, and (b,d,f) Zn deposition rate and current efficiency. (a,b) $j = -0.5$ A dm^{-2}, (c,d) $j = -3.0$ A dm^{-2}, and (e,f) $j = -5.0$ A dm^{-2}. Electrolyte composition: 0.25 M Cit, 0.20 M $ZnSO_4$, 1 g dm^{-3} gelatin, 100 g dm^{-3} SiC. $Q = 20$ C, $T = 20°C$.

factor determining the electrodeposition rate. Zinc electrodeposition proceeds, to a larger extent, through the reduction of freely solvated Zn–Cit complex molecules. The increase of RDE speed provides faster mass transport of freely solvated Zn–Cit ions, resulting in the increase of the rate of their reduction on the cathode. In contrary, higher rotation speeds of the disc cathode may shorten the residence time of ceramic NPs at the growing surface; they can be swept more easily before incorporating into the Zn matrix under such conditions. Hence, in case of electrodeposition at –3.0 A dm^{-2}, the optimal ratio between the SiC residence time and the Zn–Cit ion reduction rate is found to be at 250 rpm, thus establishing maximal SiC incorporation (Fig. 6c) together with high current efficiency of the Zn electrodeposition process (Fig. 6d).

When considering the Zn-SiC codeposition at –5.0 A dm^{-2}, the maximal SiC incorporation is observed at 450 rpm (Fig. 6e). In this case, the wt% of SiC in Zn-SiC deposits is similar for both SiC(A) and SiC(B). Thus, the number of the smaller SiC(A) NPs should be higher than that of the larger SiC(B) NPs. SiC(A) NPs are the carrier of a higher number of Zn–Cit ions adsorbed onto their surface, which is reflected in the higher Zn deposition rate and current efficiency values in the case of Zn-SiC(A) at –5.0 A dm^{-2} (Fig. 6f). Both the Zn deposition rate and current efficiency grow significantly (ca. 4 times) with the increase of RDE speed from 150 to 550 rpm, which can be explained by the conditions of diffusion-control electrodeposition occurring together with intensive hydrogen evolution. At low RDE speed, hydrogen bubbles remain more easily in the vicinity of the cathode's surface, thus hindering the electrocrystallization processes. Moreover, such low RDE rate does not ensure sufficiently high ionic mass transport to the cathode's surface, thus limiting the Zn deposition rate. Therefore, the increase of RDE speed accelerates the Zn electrodeposition rate by ensuring a faster transport of Zn–Cit ions to the cathode and sweeping of hydrogen gas bubbles, which are formed under such conditions relatively fast. Furthermore, as claimed above, the higher RDE speed may favor sweeping of SiC NPs from the cathode's surface, resulting in the decrease of the SiC content codeposited with Zn. The opposite effect is observed at –5.0 A dm^{-2} (Fig. 6e). The

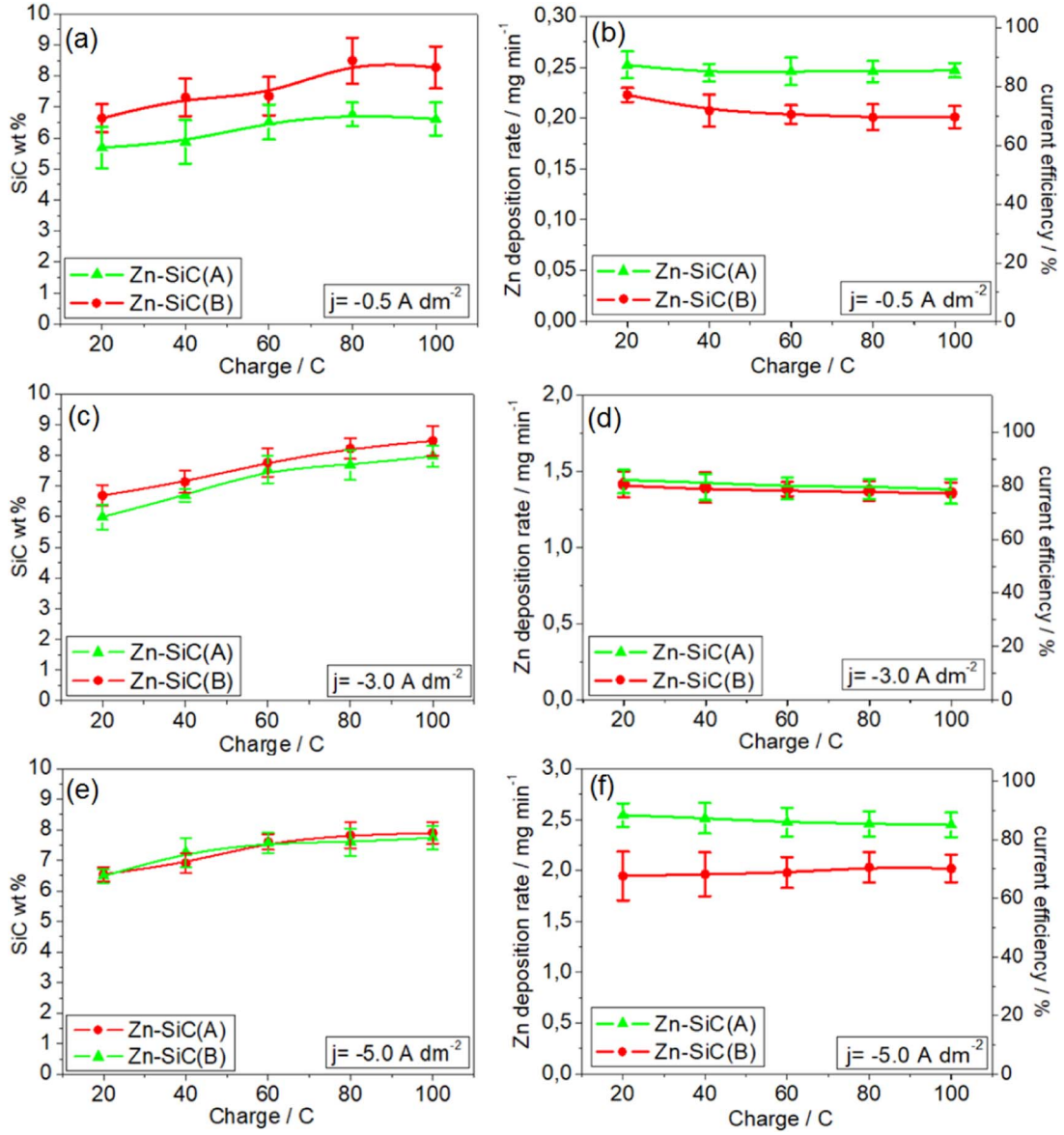

Figure 7. The effect the charge passed during electrodeposition on: (a,c,e) the SiC content in Zn-SiC composite deposits, and (b,d,f) Zn deposition rate, at three selected current densities and two rotation rates: (a,b) –0.5 A dm^{-2}, 250 rpm; (c,d) –3.0 A dm^{-2}, 250 rpm; (e,f) –5.0 A dm^{-2}, 450 rpm. Electrolyte composition: 0.25 M Cit, 0.20 M $ZnSO_4$, 1 g dm^{-3} gelatin, 100 g dm^{-3} SiC. $T = 20°C$.

observed increase in the wt% of SiC with the increase of the RDE speed may be attributed to similar values of mass concentration of SiC incorporated in both Zn-SiC(A) and Zn-SiC(B) under the same conditions. This implies that ceramic NPs are incorporated mainly not as single particles during the reduction of citrate-zinc ions firstly adsorbed on its surface, but they are entrapped into pores formed in the deposit. Under conditions of high overpotential, a relatively fast electrocrystallization accompanied with intensive hydrogen evolution favors the formation of pores, cavities and discontinuities in the deposit, and the SiC NPs may be mechanically entrapped in the deposit during the electrodeposition process. Since the surface morphology and microstructure of deposits is similar for both Zn-SiC(A) and Zn-SiC(B), as shown in the Morphological and structural studies of Zn and Zn-SiC layers and Phase analysis of Zn and Zn-SiC nanocomposite layers sections below, pores of similar average size and shape may trap a comparable mass of SiC NPs in both of the studied systems (Fig. 6e). But, the smaller SiC(A) NPs are the carrier of more Zn–Cit ions, which are reduced rapidly when reaching the cathode's surface under conditions of mass-transport control; hence, higher Zn deposition rate and current efficiency are observed in the case of Zn-SiC(A) (Fig. 6f).

The effect of the total charge passed during electrodeposition of Zn-SiC composites is shown in Fig. 7. Generally, the SiC content in the deposits grows slightly with the increase of passed charge (Figs. 7a, 7c, 7e). On the other hand, the Zn deposition rate and current efficiency values are of similar values within the whole range of total charge passed (Figs. 7b, 7d, 7f). Hence, the studied process of Zn electrodeposition is stable in both Zn-Cit-SiC(A) and Zn-Cit-SiC(B) systems, whereas the observed increase of SiC content does not influence significantly electrode processes. However, the increase of charge passed is directly related to the increase of the deposited layer thickness, the surface of which also becomes more developed with increasing deposition time, as confirmed by both macroscopic and microscopic observations (not shown here). As the surface becomes more developed and rough, the higher is the probability of the mechanical entrapment of SiC NPs in cavities. These results are in line with the statement that SiC NPs are incorporated into the Zn matrix not only as individual NPs during the reduction of Zn–Cit ions

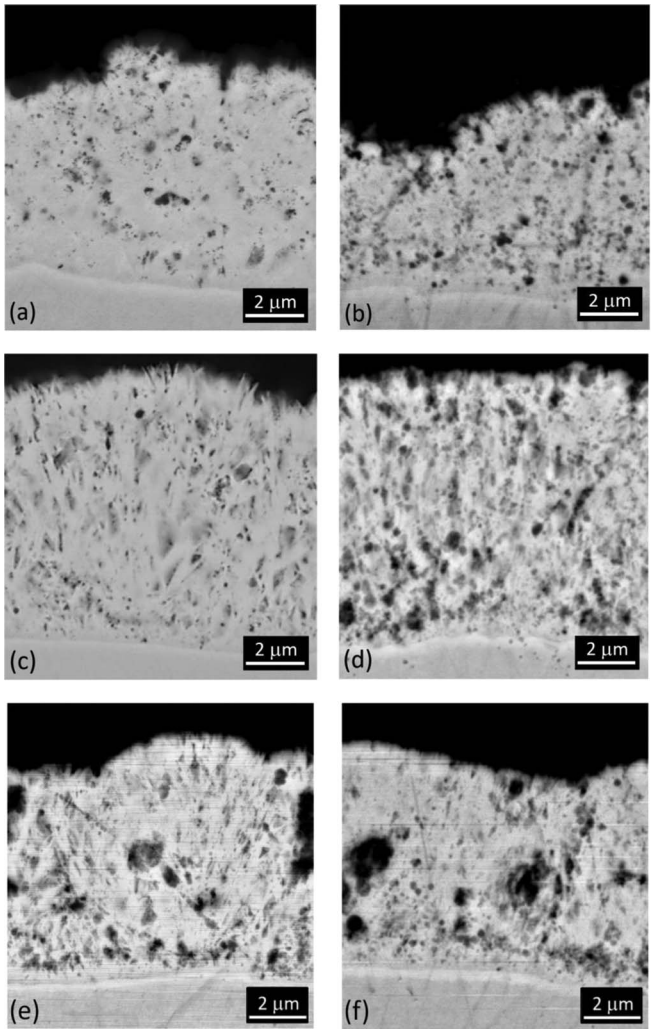

Figure 8. SEM backscatter electron (BSE) images of cross-sections of Zn–SiC layers electrodeposited at (a,b) –0.5 A dm^{-2}, (c,d) –3.0 A dm^{-2}, (e,f) –5.0 A dm^{-2}. Baths containing: (a,c,e) 60 g dm^{-3} SiC(A), (b,d,f) 60 g dm^{-3} SiC(B). $\omega = 300$ rpm, $Q = 80$ C, $T = 20°C$.

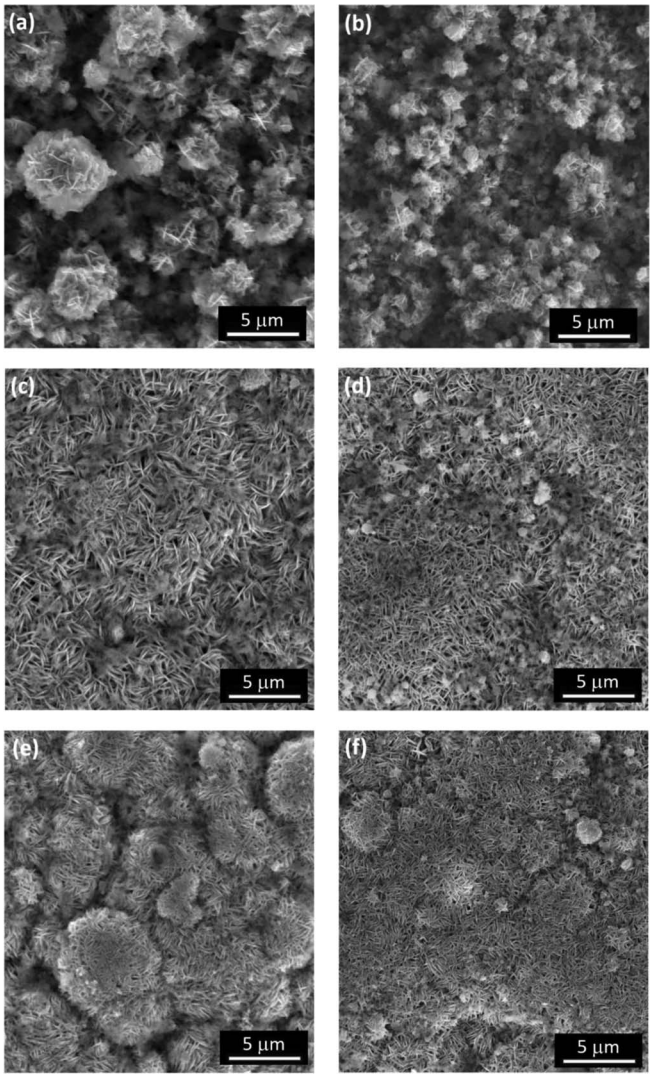

Figure 9. SEM secondary electron (SE) images revealing the surface morphologies of Zn–SiC layers electrodeposited at: (a,b) –0.5 A dm^{-2}, (c,d) –3.0 A dm^{-2}, (e,f) –5.0 A dm^{-2}. Baths containing: (a,c,e) 60 g dm^{-3} SiC(A), (b,d,f) 60 g dm^{-3} SiC(B). $\omega = 300$ rpm, $Q = 80$ C, $T = 20°C$.

initially adsorbed on their surface, but they also can be mechanically entrapped as agglomerates in the discontinuities and pores formed in the deposit.

Morphological and structural studies of Zn and Zn-SiC layers.— SEM images of cross-sections of Zn-SiC(A) and Zn-SiC(B) coatings are presented in Fig. 8. The distribution of incorporated particles is similar for both the Zn-SiC(A) and Zn-SiC(B) systems. The particles are distributed relatively uniformly in the whole volume of the Zn layers in the form of single particles as well as in the form of agglomerates of different sizes. Both composite coatings obtained at –5.0 A dm^{-2} show a thin region, close to the substrate's surface, depleted in SiC. Next, a slightly gradient structure with a higher concentration of SiC particles close to the pure zinc region in the vicinity of the substrate can be observed (Figs. 8e, 8f). This confirms that under such condition of high overpotential, the Zn electrodeposition process proceeds mainly by the reduction of freely solvated Zn–Cit ions, hence the layer of pure zinc is deposited first. Next, when the cathode's surface becomes more developed as a result of fast electrocrystallization of Zn and intensive hydrogen evolution, the SiC NPs start to be incorporated into the structure. The SiC particles are incorporated in the form of relatively large agglomerates. This observation confirms that at –5.0 A dm^{-2}, a condition of high overpotential, the ratio between the growth rate of Zn and SiC residence time does not support the codeposition of SiC in the form of single NPs. If the growth rate of Zn is too high and the residence time of SiC is too low, it can be related to the high rate of hydrogen evolution under such conditions, which causes detachment of NPs from the cathode surface before their embedment into the growing Zn layer. On the other hand, high rate of Zn deposition together with intensive hydrogen evolution results in the formation of a non-uniform deposit. Then, the incorporation of SiC takes place, to a large extent, by the mechanical entrapment of SiC agglomerates in the pores, cavities and other defects created during the formation of the deposit (Figs. 8e, 8f). A significantly lower number of the cavities filled with SiC aggregates can be noticed within the coating deposited at lower overpotentials (Figs. 8a–8d); however, some SiC agglomerates are still observed, implying that the mechanism of the mechanical entrapment of SiC aggregates may accompany the Zn-SiC codeposition process within the whole range of current-potential values studied. Such results indicate that the SiC NPs are not distributed properly in the solution, so that agglomerates may be formed in it. However, significantly higher amounts of agglomerates, incorporated into Zn matrix under conditions of high cathodic currents, suggest also that these conditions favor the formation of agglomerates.

The surface morphology is very similar for both Zn-SiC(A) and Zn-SiC(B) systems (Fig. 9); it depends mainly on the value of the applied current density. The coatings deposited at –0.5 A dm^{-2} exhibit

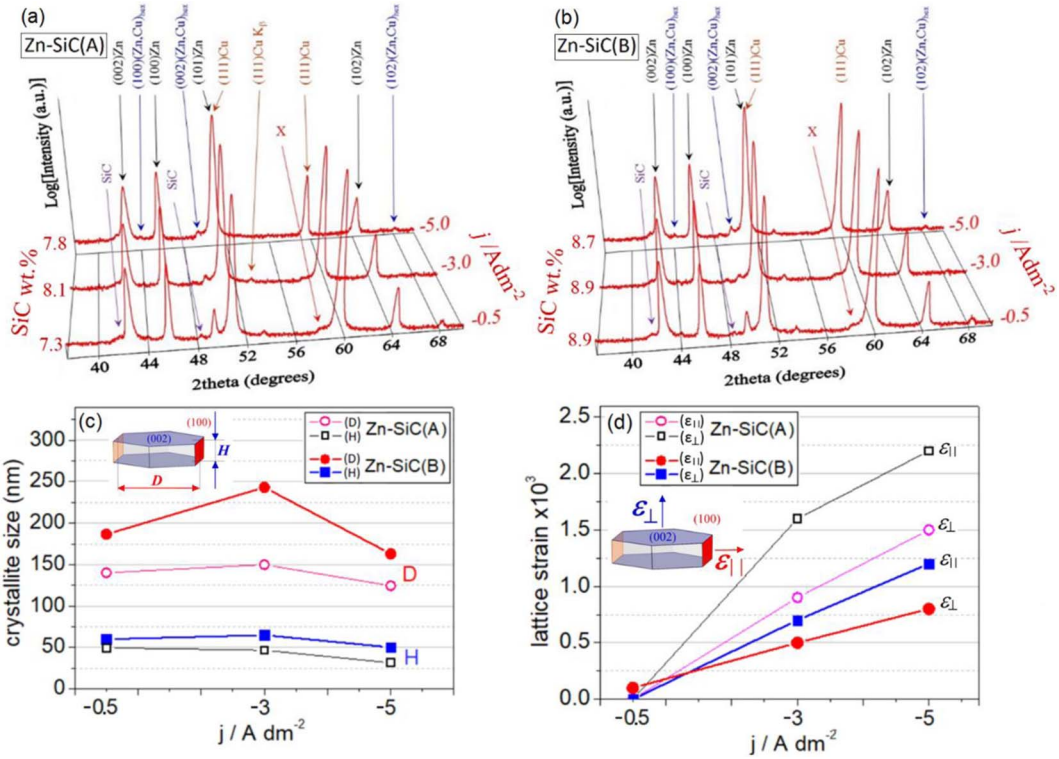

Figure 10. XRD patterns of (a) Zn-SiC(A), (b) Zn-SiC(B) layers electrodeposited at three selected values of current density. Electrolyte composition: 0.25 M Cit, 0.20 M $ZnSO_4$, 1 g dm^{-3} gelatin, 60 g dm^{-3} SiC. (c) The change in crystallite size as a function of applied current density in terms of: H – crystallite height, and D – crystallite diameter, determined from the analysis of the peak profiles of reflections (002) and (100), respectively. (d) The change in lattice strain as a function of applied current density. *D* parameter values > 100 nm are determined based on an assumption as in Ref. 46.

developed nodular structures, both in Zn-SiC(A) and in Zn-SiC(B) deposits. However, these nodules consist of smaller needle-like grains (Figs. 9a, 9b). On the other hand, Zn-SiC composite layers obtained at –3.0 A dm^{-2} exhibit significantly smoother surfaces with needle-like structure (Figs. 9c, 9d). The morphology of deposits obtained at –5.0 A dm^{-2} is similar to that observed at –3.0 A dm^{-2}, but with slightly smaller size of the needle-like grains. Moreover, the surfaces of layers deposited at –5.0 A dm^{-2} are slightly more developed (more porous and rougher), which is expected with a higher rate of hydrogen evolution (Figs. 9e, 9f). The higher Zn deposition rate in the case of the Zn-SiC(A) (Fig. 5c) system leads to more developed surface morphology in comparison to Zn-SiC(B). Dark gray, blurry spots visible on the BSE SEM images of the coating surface (not shown here) confirm the presence of some SiC agglomerates at the surface of each deposit.

The surface morphologies formed in the Zn-Cit-SiC(B) system (Figs. 9b, 9d, 9f) consist of slightly smaller grains in comparison to those of Zn-Cit-SiC(A) (Figs. 9a, 9c, 9d). However, it should be noted that the word "grain" in this context does not refer directly to the crystallites, but to the structures created during electrodeposition (which may be composed of crystallites of different size) that form the characteristic topography of the deposited layers. To estimate the actual crystallite size of deposits, XRD measurements were performed; the results are described in Phase analysis of Zn and Zn-SiC nanocomposite layers section.

Phase analysis of Zn and Zn-SiC nanocomposite layers.—Fig. 10 shows the XRD patterns of Zn-SiC coatings with the two types of SiC NPs, electrodeposited at three selected current densities. In all cases considered, XRD analysis reveals the presence of hexagonal zinc (Zn), hexagonal zinc enriched with Cu $(Zn,Cu)_{hex}$, SiC, and the copper substrate. Peaks corresponding to SiC are visible in the diffractograms acquired for the Zn-SiC systems (Figs. 10a, 10c).

It can be argued that the changes in the applied current density and the SiC NP types do not have a significant effect on the phase composition of the electrodeposited Zn-SiC composite coatings, although there are some changes in crystallite size. The crystallite size is noticeably smaller for Zn-SiC(A) coatings than for Zn-SiC(B) deposits (Fig. 10c). This can be explained if SiC NPs act as nucleation sites. The average crystallite size is affected by the competition between nucleation and growth. When either the density of nucleation sites or the nucleation rate increases, the mean crystallite size decreases.[45] A higher number of the smaller SiC(A) NPs provides more nucleation sites compared to the lower number of the larger SiC(B) NPs, for the same concentration of ceramic particles in the bath. A higher number of nucleation sites combined with a higher electrodeposition rate thus yield smaller crystallites in the Zn-Cit-SiC(A) system (see Figs. 5–7).

The lattice strain of composite coatings depends both on the applied current density and the mean size of SiC NPs incorporated (Fig. 10d). There is only negligible internal strain in the Zn matrix deposited at the lowest overpotential (at –0.5 A dm^{-2}), when the Zn deposition rate is very low (Fig. 5c) and SiC codeposition takes place at the potential of zero charge, E_{pzc}.[26] It can be concluded that under such condition, Zn crystallites grow slowly around SiC NPs, which do not cause any noticeable lattice strain. In cases of layers deposited at –3.0 and –5.0 A dm^{-2}, the lattice strain increases with both the increase of cathodic current density and the decrease in the average size of SiC NPs incorporated into the Zn matrix. This can be associated with mismatching stress between the matrix and the SiC.[46] The noted internal stresses are higher in the case of Zn-SiC(A), even though the overall SiC content in the composite layer is lower in Zn-SiC(A) compared to Zn-SiC(B) (Figs. 10a, 10b). However, due to the smaller average size of SiC(A) NPs, the expected number of NPs embedded into the Zn matrix is higher (Fig. 10c). Consequently, the strain increases when the SiC NPs are introduced into the finer grained Zn matrix. The

higher number of SiC NPs incorporated into a finer Zn microstructure (Fig. 10c) results in lattice mismatch and, consequently, in induced stresses between SiC and Zn.

Conclusions

- Comparison was made between the codeposition behavior of Zn with SiC NPs of two average sizes: 56 nm (SiC(A)) and 90 nm (SiC(B)). The dependences of SiC wt% on the current density, hydrodynamic conditions, and the total charge passed is similar for both SiC systems. The noticeably higher content of SiC observed in Zn-SiC(B) deposits is associated with the larger average size of NPs incorporated into the Zn matrix. This result along with the generally higher Zn deposition rate and current efficiency observed in the case of codeposition of the smaller SiC(A) confirm that SiC NPs are the carrier of Zn–Cit, which is then reduced on the cathode's surface.
- Zn-SiC incorporation may proceed during the reduction of citrate-zinc ions that are first adsorbed on their surface as well as by mechanical entrapment of NP agglomerates in cavities and pores in the deposit. The mechanism of SiC codeposition during the reduction of the adsorbed ions surrounding them is favorable under conditions of low overpotential and low RDE speed, which ensure a relatively slow, activation-controlled, Zn electrodeposition process and sufficiently long residence time of SiC NPs on the cathode's surface. This allows their incorporation into the growing metal matrix. The mechanism of mechanical entrapment of SiC in the form of agglomerates becomes more significant at higher overpotential, when a relatively fast, diffusion-controlled, Zn electrodeposition process is accompanied by high rate of hydrogen evolution, resulting in the formation of non-uniform Zn deposit with pores and cavities.
- Both the applied current density and the mean size of the SiC NPs do not have a significant influence on the phase composition of the electrodeposited Zn–SiC composite coatings. The microstructure typically consists of hexagonal Zn, with some additional phases associated with the diffusion of copper from the substrate. The crystallite size is smaller in Zn–SiC(A) layers than in Zn–SiC(B) layers, suggesting that SiC NPs surrounded by Zn–Cit ions may act as nucleation sites for zinc electrocrystallization.
- The lattice strain in the Zn–SiC coating depends both on the applied current density and the mean size of incorporated SiC NPs. No noticeable strain is evident in coatings deposited at –0.5 A dm^{-2}. However, the strain increases as the cathodic current density is increased or as the SiC size is decreased.

Acknowledgments

The research was initiated and mainly conducted within the framework of project No. LIDER/007/151/L-5/13/NCBR/2014 financed by the National Centre for Research and Development in Poland. The cooperation between the Institute of Metallurgy and Materials Science of the Polish Academy of Sciences and Tel-Aviv University was enabled thanks to COST Action MP1407 (e-MINDS). The authors gratefully acknowledge Dr. Remigiusz Kowalik for the possibility to carry out WDXRF measurements at AGH University of Science and Technology (Krakow, Poland).

ORCID

Honorata Kazimierczak https://orcid.org/0000-0001-9152-0041
Noam Eliaz https://orcid.org/0000-0002-1184-4706

References

1. N. Eliaz and E. Gileadi, *Physical Electrochemistry: Fundamentals, Techniques, and Applications*, 2nd ed., ISBN: 978-3-527-34139-9, Wiley-VCH, Germany (2019).
2. V. B. Singh and D. K. Singh, *Nanosci. Technol.*, **1**, 1 (2014).
3. D. K. Singh and V. B. Singh, *J. Electrochem. Soc.*, **158**, D114 (2011).
4. F. Kilic, H. Gul, S. Aslan, A. Alp, and H. Akbulut, *Colloids Surf. A*, **419**, 53 (2013).
5. M. Sajjadnejad, H. Omidvar, M. Javanbakht, R. Pooladi, and A. Mozafari, *Trans. Inst. Met. Finish.*, **92**, 227 (2014).
6. M. K. P. Kumar, T. V. Venkatesha, and M. K. Pavithra, *Int. J. Electrochem. Sci. Eng.*, **5**, 25 (2015).
7. S. Singh, M. Sribalaji, N. P. Wasekar, S. Joshi, G. Sundararajan, R. Singh, and A. K. Keshri, *Appl. Surf. Sci.*, **364**, 264 (2016).
8. F. C. Walsh and C. Ponce de Leon, *Trans. Inst. Metal Finish.*, **92**, 83 (2014).
9. P. Nowak, R. P. Socha, M. Kaisheva, J. Fransaer, J.-P. Celis, and Z. Stoinov, *J. Appl. Electrochem.*, **30**, 429 (2000).
10. L. Benea, P. L. Bonora, A. Borello, and S. Martelli, *Wear*, **249**, 995 (2002).
11. H. Wang, S. Yao, and S. Matsumara, *J. Mater. Process. Technol.*, **145**, 299 (2004).
12. M. D. Ger, *Mater. Chem. Phys.*, **87**, 67 (2004).
13. H. K. Lee, H. Y. Lee, and J.-M. Jeon, *Surf. Coat. Technol.*, **201**, 4711 (2007).
14. P. Gyftou, E. A. Pavlatou, and N. Spyrellis, *Appl. Surf. Sci.*, **254**, 5910 (2008).
15. I. Dobosz, E. Rudnik, and L. Burzynska, *Arch. Metall. Mater.*, **56**, 665 (2011).
16. P. Narasimman, M. Pushpavanam, and V. M. Periasamy, *Port. Electrochim. Acta.*, **30**, 1 (2012).
17. Y. H. Ahmad and A. M. A. Mohamed, *Int. J. Electrochem. Sci.*, **9**, 1942 (2014).
18. W. Q. Liu, W. N. Lei, C. Ye Wang, H. F. Qian, and L. H. Ding, *Integr. Ferroelectr.*, **167**, 192 (2015).
19. M. Sajjadnejad, A. Mozafari, H. Omidvar, and M. Javanbakht, *Appl. Surf. Sci.*, **300**, 1 (2014).
20. G. Roventi, G. Giuliani, M. Pisani, and T. Bellezze, *Int. J. Electrochem. Sci.*, **12**, 663 (2017).
21. G. Roventi, T. Bellezze, and R. Fratesi, *J. Appl. Electrochem.*, **43**, 839 (2013).
22. N. Haghmoradi, C. Dehghanian, and S. Yari, *J. Mater. Eng. Perform.*, **25**, 3746 (2016).
23. C. Muller, M. Sarret, and M. Benballa, *Surf. Coat. Technol.*, **162**, 49 (2003).
24. P. C. Tulio, S. E. B. Rodrigues, and I. A. Carlos, *Surf. Coat. Technol.*, **202**, 91 (2007).
25. P. C. Tulio and I. A. Carlos, *J. Appl. Electrochem.*, **39**, 1305 (2009).
26. H. Kazimierczak, K. Szymkiewicz, L. Rogal, E. Gileadi, and N. Eliaz, *J. Electrochem. Soc.*, **165**, D526 (2018).
27. W. D. Callister, *Materials Science and Engineering. An introduction*, John Wiley & Sons, Inc. (2007).
28. C. T. J. Low, R. G. A. Wills, and F. C. Walsh, *Surf. Coat. Technol.*, **201**, 371 (2006).
29. P. M. Vereecken, I. Shao, and P. C. Searson, *J. Electrochem. Soc.*, **147**, 2572 (2000).
30. N. Gugliemi, *J. Electrochem. Soc.*, **119**, 1009 (1972).
31. J. P. Celis, J. R. Roos, C. Buelens, and J. Fransaer, *Trans. Inst. Met. Finish.*, **69**, 133 (1991).
32. J. Fransaer, J. P. Celis, and J. R. Roos, *J. Electrochem. Soc.*, **139**, 413 (1992).
33. G. Maurin and A. Lavanant, *J. Appl. Electrochem.*, **25**, 1113 (1995).
34. B. J. Hwang and C. S. Hwang, *J. Electrochem. Soc.*, **140**, 979 (1993).
35. D. Eroglu and A. C. West, *J. Electrochem. Soc.*, **160**, D354 (2013).
36. M. Pushpavanam and K. Balakrishnan, *J. Appl. Electrochem.*, **26**, 1065 (1996).
37. H. Kazimierczak, P. Ozga, A. Jalowiec, and R. Kowalik, *Surf. Coat. Technol.*, **240**, 311 (2014).
38. H. Kazimierczak, P. Ozga, M. Slupska, Z. Swiatek, and K. Berent, *J. Electrochem. Soc.*, **161**, D309 (2014).
39. R. J. Hunter, *Zeta Potential in Colloid Science*, New York: Academic Press (1981).
40. A. LeBail, H. Duroy, and J. L. Fourquet, *Mater. Res. Bull.*, **23**, 447 (1988).
41. J. Rodriguez-Carvajal, *Physica B*. **192**, 55 (1993).
42. Th. H. de Keijser, J. I. Langford, E. J. Mittemeijer, and A. B. P. Vogels, *J. Appl. Cryst.*, **15**, 308 (1982).
43. M. Kosmulski, *Surface Charging and Points of Zero Charge*, Boca Raton, FL: CRC Press (2009).
44. C. R. Carpenter, P. H. Shipway, and Y. Zhu, *Surf. Coat. Technol.*, **205**, 5059 (2011).
45. Y. L. Yang, Y. D. Wang, Y. Ren, C. S. He, J. N. Deng, J. Nan, J. G. Chen, and L. Zuo, *Mater. Lett.*, **62**, 45 (2008).
46. F. T. L. Muniz, M. A. Ribeiro Miranda, C. Morilla dos Santos, and J. M. Sasaki, *Acta Cryst. A*, **72**, 385 (2016).